Electronic and transport properties of two-dimensional conjugated polymer networks including disorder.

Jean-Joseph Adjizian,[*,†,‡] Aurélien Lherbier,[†,‡] Simon Dubois,[†] Andrés Rafael Botello-Méndez,[†] and Jean-Christophe Charlier[†]

† *Université catholique de Louvain, Institute of Condensed Matter and Nanosciences, Chemin des étoiles 8, 1348 Louvain-la-neuve, Belgium*

‡ *The first two authors, JJA and AL, contributed equally to this work*

E-mail: jean.adjizian@uclouvain.be

Abstract

Two-dimensional (2D) conjugated polymers exhibit electronic structures analogous to that of graphene with the peculiarity of $\pi - \pi^*$ bands which are fully symmetric and isolated. In the present letter, the suitability of these materials for electronic applications is analyzed and discussed. In particular, realistic 2D conjugated polymer networks with structural disorder such as monomer vacancies are investigated. Indeed, during bottom-up synthesis, these irregularities are unavoidable and their impact on the electronic properties are investigated using both *ab initio* and *tight-binding* techniques. The *tight-binding* model is combined with a real space Kubo-Greenwood approach for the prediction of transport characteristics for monomer vacancy concentrations ranging from 0.5% to 2%. As expected, long mean free paths and high mobilities are predicted for low defect densities. At low temperatures and for high defect densities, strong localization phenomena originating from quantum interferences of multiple scattering paths are observed in the close vicinity of the Dirac energy region while the absence of localization effects is predicted away from this region suggesting a sharp mobility transition. These predictions show that 2D conjugated polymer networks are good candidates to pave the way to the ultimate scaling and performances of future molecular nanoelectronic devices.

Keywords

2DCP, DFT, Tight-Binding, Transport, Localization

Introduction

The electronic structure of graphene exhibits no band gap at the Fermi level but rather a linear dispersion at the K-points of the Brillouin zone. The latter means that low energy carriers behave like free relativistic massless particles as described by the Dirac equation.[1,2] Such a particular electronic structure is a direct consequence of the underlying hexagonal lattice composed of two symmetrically equivalent triangular sub-lattices.[3] The outstanding properties of graphene resulting from its exotic Dirac carriers have sprung a large interest, and important efforts have been focused on tuning these properties. Among others, a popular approach to modify the electronic structure of graphene Dirac carriers, and in particular to open a band gap, has been through confinement in the so-called graphene nanoribbons (GNRs). In this direction, a breakthrough has come from the bottom-up synthesis of GNRs from the self-assembly of organic precursors.[4] Such an approach yields GNRs with well defined edges and well defined width, thus allowing an *a priori* knowledge of their properties. Similarly, it was recently shown that a careful choice of monomers could result in the bottom-up synthesis of two-dimensional conjugated polymer (2DCP) networks with Dirac cones at or near the Fermi level.[5] These 2DCP networks can be described by the three fold connection of a wide range of short one dimensional (1D) conjugated polymer chains. With the structural similarities between covalent organic frameworks (COFs)[6,7] and 2DCPs, the advanced bottom-up chemistry strategies developed for COFs have been adapted for the synthesis of 2DCPs, thus leading to the first 2DCP synthesis using tris(4-bromophenyl)amine molecules as monomer precursors.[8,9] Given the set of potential 2D architectures, chemical constituents, and functional modifications, 2DCP networks represent an interesting playground to tune the properties of Dirac carriers. In addition, they should be highly flexible and adjustable to a wide range of fundamental and applied problems.[10,11]

In this paper, the electronic and transport properties of 2DCPs are investigated using first-principles techniques and an accurate *tight-binding* model combined with an efficient real space Kubo-Greenwood transport formalism. The poly(p-phenylene) (PPP)-based 2D-C-$(PP_1)_3$ was chosen as a representative member of 2DCPs. It displays an electronic structure similar to graphene with massless Dirac-like fermions but on an energy scale almost ten times smaller.[5] Electronic transport in defective graphene has already been experimentally measured and theoretically investigated[12–15] revealing the importance of structural disorder on the transport performances. Because synthesizing 2DCPs with a bottom-up approach will inevitably introduce structural defects, it is important to study how such defects will affect transport behavior in 2DCPs. In particular, monomer vacancies randomly distributed in the honeycomb lattice of a mesoscopic size 2DCP are considered in the present study. The real-space Kubo-Greenwood transport formalism allows to explore all transport regimes, including quantum localization effects beyond the semi-classical approximation in realistic size systems. Rather long mean free paths and high mobilities are predicted for low defect densities, indicating the good potential of 2DCP-based nanoelectronic devices. Interestingly, at high defect densities, strong localization phenomena originating from quantum interferences of multiple scattering paths are observed in the close vicinity of the Dirac energy region while the absence of localization effects is predicted away from this region with a sharp transition between both regions. This suggests an observable mobility edge at low temperature measurement, which in commonly believed to occur only in 3D systems.[16] This theoretical work conveys insights onto these new 2D materials and motivates for their experimental synthesis and transport measurements.

Results and discussion

Tight binding parameterization

First-principles calculations were conducted to obtain the optimized geometry and electronic spectrum of the PPP-based 2D-C-$(PP_1)_3$. The electronic structure calculations were first carried out using the self-consistent density functional theory (DFT) method implemented in the SIESTA package[17,18] (see method section for details).

Figure 1A (top panel) illustrates the atomic structure of 2D-C-$(PP_1)_3$. As mentioned already, such 2D networks can be obtained by the self-assembly of monomer precursors. The monomer precursor is composed of the connector atom plus three short polymer chains. In the present case, the chain is reduced to one benzene ring for simplicity and the connector is a carbon atom (i.e. C-$(PP_1)_3$). The main difference between the studied 2DCP and the experimentally available analogue (2D-N-$(PP_1)_3$)[8,9] is the nature of the connector atoms, which in this case is a nitrogen atom. Carbon connectors have been chosen in this study as they have the peculiarity to result in a Dirac cone directly at the Fermi energy while the nitrogen connectors, first used in synthesis experiments, tend to shift the Fermi level to higher energies. It is anticipated that 2DCPs with various connectors, including carbon connectors, will be synthesized in a near future.

Despite the atomic accuracy of the bottom-up synthesis strategy, faults will ineluctably occur in the self-assembly resulting in structural defects. In this study, monomer vacancies

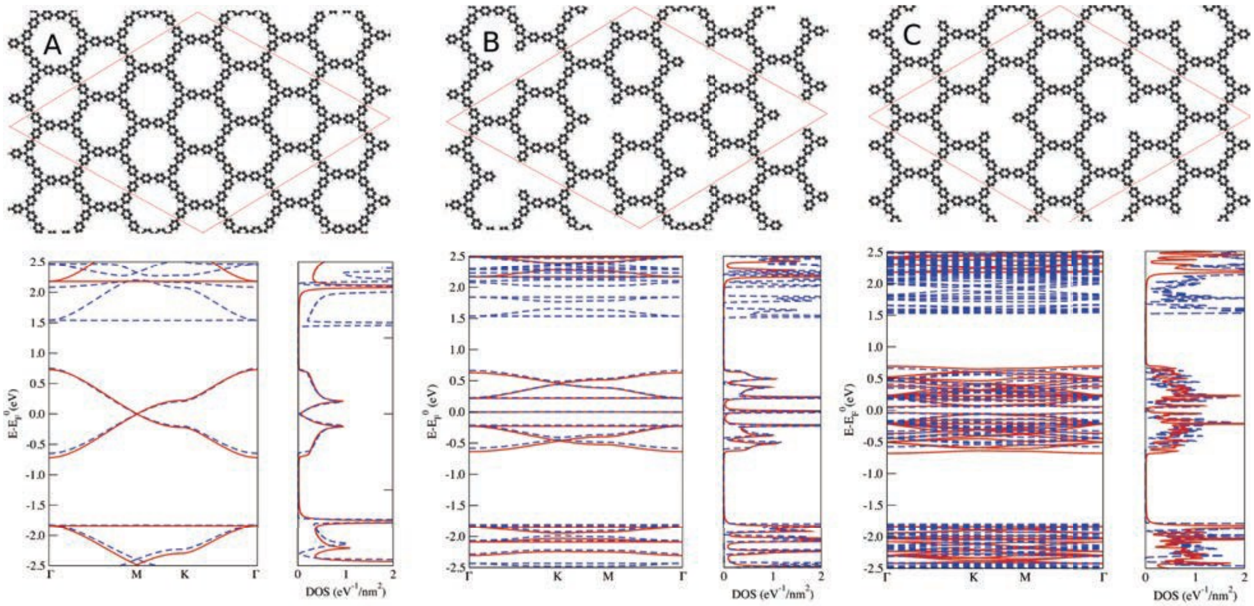

Figure 1: Top: Inside the red cell, 4×4 super cells for a pristine 2DCP in (A), containing four monovacancies (12.5%) in (B) and containing two monovacancies (6.25%) with an equivalent number on both sub-lattices in (C). Bottom: *ab initio* (dashed blue line) and *tight-binding* (red thick line) band structures and densities of states (DOS) of the corresponding atomic structures (A), (B), and (C). The Fermi energy is aligned with E=0 eV.

are considered as prototypical structural defects. To get a first insight on the impact of monomer vacancies on the low-energy electronic structure, small 2D-C-$(PP_1)_3$ super cells containing few defects were first investigated (see Figs. 1B-C).

The band structures and densities of states (DOS) corresponding to the pristine and defective 2D-C-$(PP_1)_3$ are reported in Figure 1 (bottom panels). To estimate the percentage of defects, the number of vacancies per cell is calculated. Each monomer vacancy corresponds to a monomer precursor missing. For example, in a pristine 2×2 cell, there are eight monomers, if one single-monomer vacancy is created in this cell, the concentration of defects n_v becomes 12.5%. The equilibrium Fermi level (E_F^0) is taken as energy reference. Figure 1 compares the band structures computed from first-principles (dotted blue lines) with results obtained from an adjusted *tight-binding* (TB) model (red lines). In this orthogonal third nearest neighbors $\pi - \pi^*$ TB model, the hydrogen atoms are not explicitly accounted for.

Instead, the hydrogenated carbon on-site energies are modified to integrate out the hydrogen neighbors (as routinely performed for instance in TB models of GNRs). The parameters of the TB model, i.e. the on-site terms (ϵ_{p_z}) and hopping terms (γ(d)), are summarized in Table 1. Further details are given in the methodology section. As shown in Figure 1, a very good agreement is achieved for the low-energy spectrum of both the pristine and the defective 2D-C-$(PP_1)_3$ especially in the region close to the Fermi energy. The dispersion relations of the high-energy conduction bands is similarly accurate but the TB approximations come with a shift of these bands to higher energies.

At low energies, the pristine 2DCP presents a band structure and DOS very similar to the one of graphene but on a different energy scale (see Fig. 1A). An almost symmetric π-π^* bands is reported with a linear dispersion in the vicinity of the Fermi energy, forming a Dirac cone. These π-π^* bands encompass an energy window of approximately 1.5 eV, that is roughly ten times smaller than in the graphene spectrum. The low energy bands are isolated from the rest of the spectrum (and in particular from the σ bands) by energy gaps of $\sim$ 1.5-2.0 eV. Plotting the wave-functions for the highest occupied band (see Fig. 1 in supplementary materials) reveals that the states are dispersed over the whole 2DCP skeleton which is a typical signature of 2D conjugated polymers. However, these *ab initio* calculations are carried at 0K, and at room temperature, benzene rings will have the freedom to rotate. In order to understand the effect of such rotation, dihedral angles have been tuned manually for a given branch or a single benzene ring. Figure 2 in supplementary materials illustrates the four possible situations. For each structure, the electronic band structure was calculated and displayed using a specific path in the Brillouin zone. These results clearly demonstrate that the electronic properties for the $\pi - \pi^*$ bands are not strongly affected by the rotation of the benzene rings. The only noticeable difference concerns the shift of the Dirac cone which is observed to be slightly delocalized from the high symmetry K-point of the Brillouin zone. A similar behavior has previously been observed in graphene in the presence of defects[14] and is due to ground state symmetry breaking. These ab initio calculations demonstrate the robustness of the electronic properties and specially the conservation of the Dirac cone at higher temperature, and further highlight the possible use of these quasi-2D conjugated polymer network for different nanoelectronic applications.

The band structure of a 2×2 super cell containing a single monomer vacancy (i.e. a concentration of n_v=12.5%) is displayed in Figure 1B. Flat band associated with defect-induced localized states are reported around the Fermi level. Narrow band gaps are observed on each sides of the zero energy mode and the band structure conserves an overall mirror symmetry between valence and conduction bands. From the emergence of a zero energy mode, it is straightforward to anticipate that electronic transport will be mainly affected in an energy window around the Fermi level. However, one has to stress out that the peculiar band structure reported in Figure 1B results directly from the periodic boundary conditions imposed on the system. In this configuration, vacancies form a regular super-lattice affecting exclusively one of the two triangular monomer sub-lattices of the pristine 2DCP. It has already been demonstrated for graphene that having local disorder either on only one or on both sub-lattices changes qualitatively the low energy spectrum.[12,19,20] To understand if a similar behavior is observed in 2DCP, larger super-cells have been considered where the monomer vacancies impact both sub-lattices. Such a case, a 4×4 super-cell containing one monomer vacancy on each sub-lattice (n_v=6.25%) is illustrated in Figure 1C. The emergence of defect induced flat bands in the low energy spectrum appears clearly in the DOS and the mirror symmetry between valence and conduction bands is maintained. However, one notes the absence of a central peak and note instead the presence of an unique small gap. Further consideration of different vacancies arrangement but still preserving the balance in sub-lattice disorder (see Fig. 3 in supplementary materials) emphasizes the dependence of the low energy spectrum upon the detailed arrangement of defects within the periodic cell. Conclusions can be drawn from these preliminary calculations of periodic arrangements of vacancies: (i) there is no zero mode observed in the case of compensated sub-lattices as compared to the fully uncompensated case reported in Figure 1B, (ii) the width of the so-induced energy gaps depends on the detailed atomic configuration. An enlightening discussion of the emergence/absence of zero energy modes in honeycomb lattices can be found in Ref. 12.

Transport properties

Larger disordered super-cells are required to capture the physics of defective mesoscopic 2DCP samples. Figure 2 depicts the atomic structure and DOS of disordered 8×8 and 16×16 super-cell containing n_v=6.25% of defects with compensated sub-lattices. While the 4×4 super cell displayed a noisy DOS whose positions of the peaks depend on the actual atomic structure (Fig.1C and Fig.3 in supplementary materials), these features are progressively averaged out as the system becomes larger as observed already for the 8×8 super cell DOS. Eventually, the 16×16 super cell exhibits a small hump in the DOS around the Fermi level associated with the overlap of defect-induced localized states whose resonant energy is very close to the Fermi level. Overall, 2DCPs show a similar behavior as graphene upon inclusion of vacancies.[12,15] When vacancies are located on one sub-lattice, the corresponding symmetry is broken, and a gap is observed on both side of the Fermi level. Zero energy modes are also observed through the sharps peaks at the Fermi energy. When vacancies are randomly distributed, it follows the theorem described in Ref. 21, and the gap on each side of the Fermi level disappear and a broader central peak is observed.

Transport properties of this defective 2DCP are then investigated, and it is important to consider the charge and discharge of the system as it would be associated under the application of a gate voltage. The transport approach is based on linear response approximation within a real-space Kubo-Greenwood methodology, where the filling in electrons or holes is accounted for as a rigid shift of the Fermi energy (E_F) with respect to the equilibrium Fermi energy position (E_F^0). As reported in Figure 3, the rigid shift model provides a very good

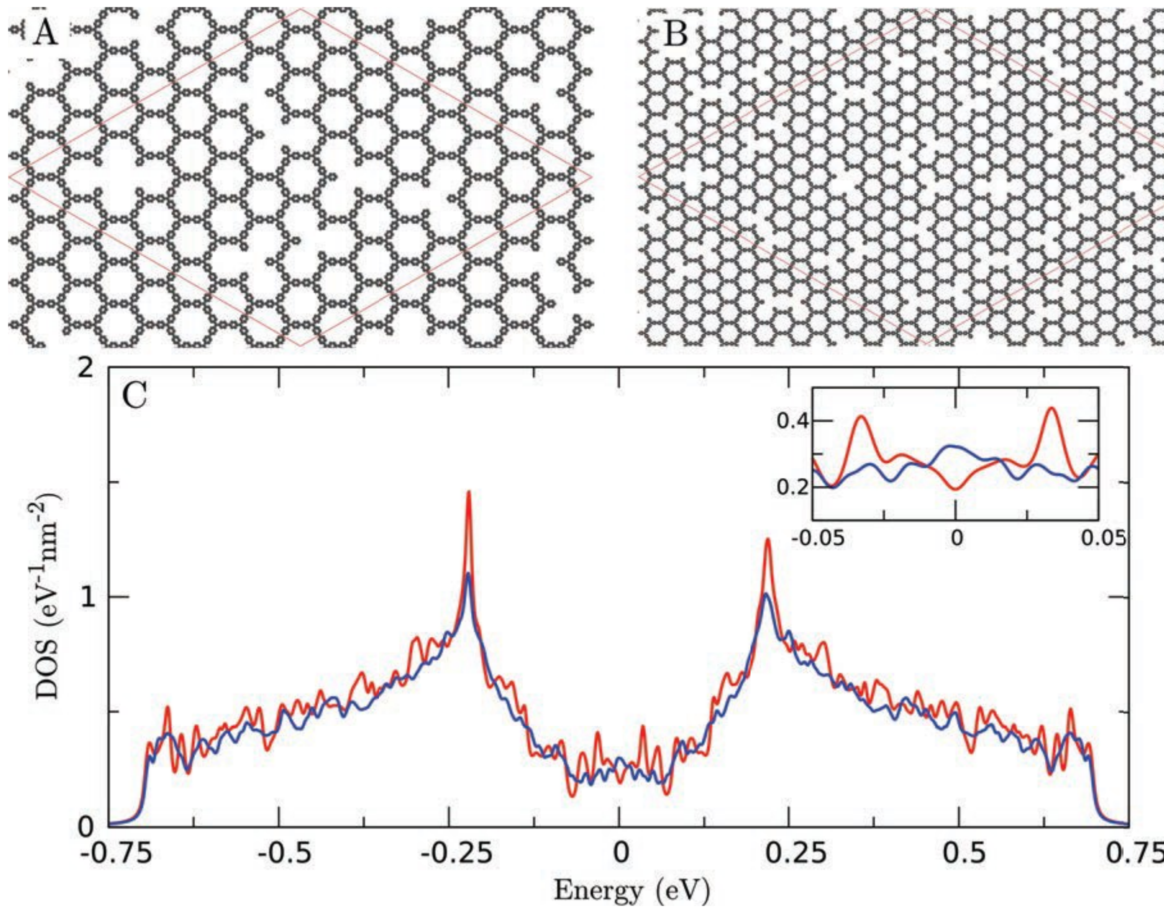

Figure 2: (A) Atomic structures of defective 2DCP: 8×8 (A) and A 16×16 (B) super-cell containing 6.25% of vacancies (with the same number of vacancies on each sub-lattice), (C) The respective DOS for A (red) and B (blue) (Inset is a zoom in at the Fermi level).

approximation for the charge/discharge in such conjugated polymer crystals. Figure 3 shows the impact on the electronic band structure of adding and removing electrons from pristine 2D-C-$(PP_1)_3$. Here, a background charge density has been added to the first-principles calculations in order to preserve overall charge neutrality as is commonly done to simulate doped systems. Bands near the equilibrium Fermi energy (equivalently around the Dirac point) are not significantly modified by variations of the charge density up to two electrons per unit-cell which corresponds to the depletion/filling of an entire electronic band. The integrity of the system is maintained and the 2D-C$(PP_1)_3$ geometry is only slightly modified. The calculations predict change in dihedral angle of a maximum of 1.42° of the PPP branches. This stability is generally observed in carbon allotropes where the σ bonds ensure the mechanical stability.[22] Such large variation of the charge density, $\Delta n = 7.57\,10^{13}$ cm^{-2}, would correspond to a gate voltage (ΔV_g) of 12.13 V for an associated gate capacitance (C_g) of 1 μF cm^{-2} (that is approximately the gate capacitance of a 15 nm thick HfO_2 film[23]). One can therefore imagine to probe entirely the π bands in a transport experiment provided a good dielectric is used for the oxide gate. An alternative to the physical electrostatic gating with oxide substrate is the electrochemical gating. It consists in putting the system in a charged ionic solution which for 2DCPs is a suitable approach owing to their porous nature.

The transport properties of large 2D-C-$(PP_1)_3$ sheets (400×400 nm^2, containing ∼2.4 millions of atoms ignoring the hydrogens atoms) with a concentration of vacancy defects (n_v) randomly distributed in the honeycomb lattice ranging from 0.5% to 2.0% are investigated using the just-developed TB model. Since the position of monomer vacancies is random, the sub-lattice disorder is almost compensated (∼50% of defects in each sub-lattice with a maximum deviation of 5%). The DOS of these large 2DCPs, displayed in Figure 4A, are calculated using the Haydock recursion technique[24] using a set of eight random phase wavepackets and are averaged on two disorder configuration samples (note that an important

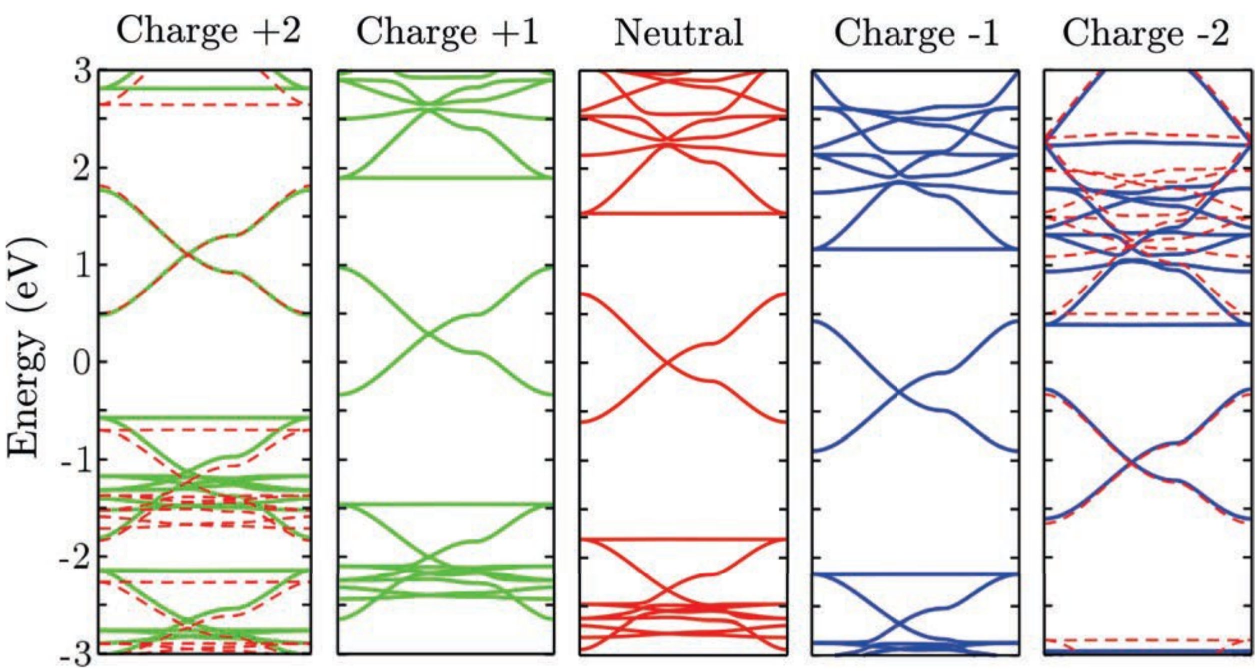

Figure 3: Electronic band structures using the simulate doping technique coded in SIESTA for a 2D-C-$(PP_1)_3$ primitive unit cell. The Fermi energy is set to zero. The band structures of positively, neutral, and negatively charged systems are plotted with green, red, and blue lines respectively. To evidence the rigid-band approximation, the shifted neutral band structure is also reported in dashed red lines in case of excess charge of -2 $| e |$ and +2$| e |$.

average over disorder configurations is already obtained within a single sample as the system is very large). As highlighted previously in Figure 2, when considering a random distribution of vacancy in a large enough 2DCP, the DOS is characterized by a small hump located at the Dirac point.

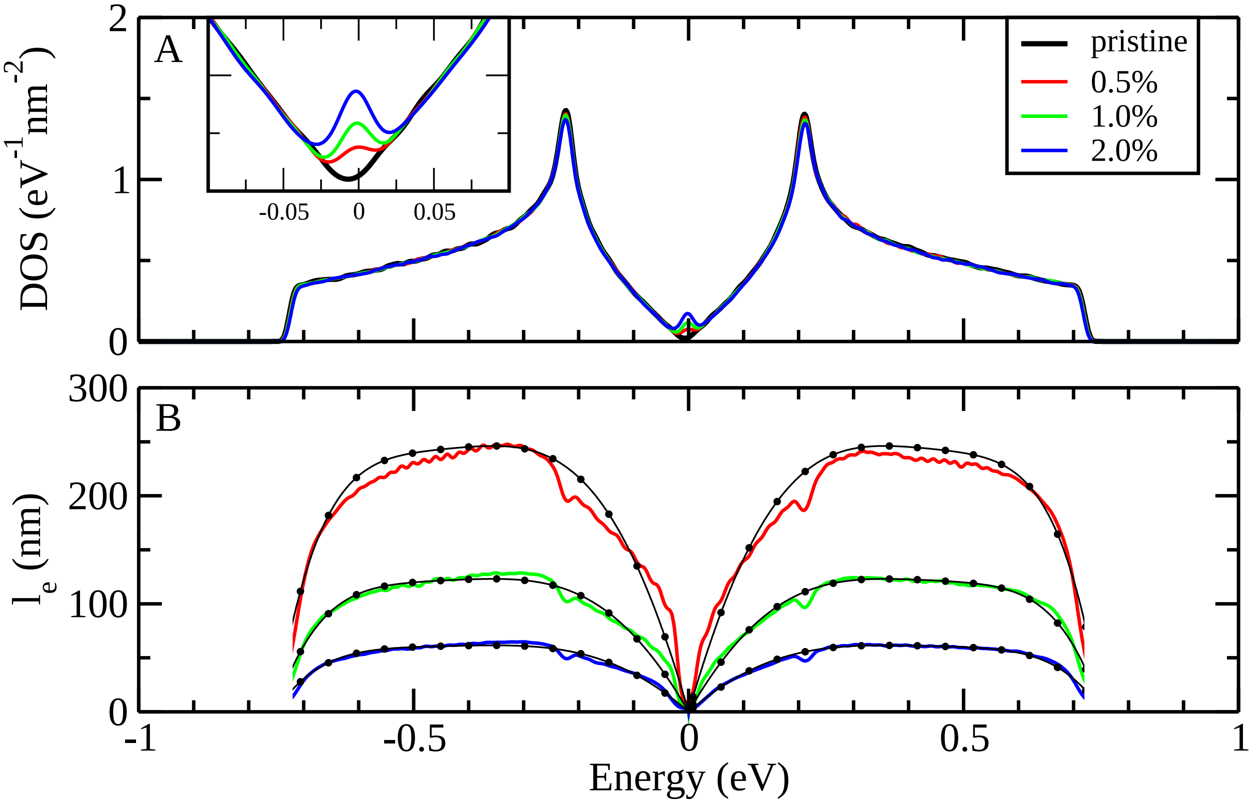

Figure 4: (A) Densities of states of 400×400 nm^2 of a 2D-C-$(PP_1)_3$ in the pristine case and with various concentrations of vacancy defects randomly distributed (0.5%,1.0%,2.0%). (B) Carrier mean free paths (l_e) of the corresponding defective 2DCP monolayers. Black dotted lines are fits obtained following the Fermi golden rule.

The time-dependent diffusivity curves D(E,t) computed within Kubo-Greenwood formalism are the signature of various transport regimes. In the semi-classical picture, the diffusivity increases and then saturates to a maximal value D^{max} in the thermodynamic limit, i.e. after a large enough number of scattering events. However, in the quantum regime, constructive interferences between scattering paths can yield localization which causes a decrease in diffusivity. Eventually, for long enough propagation time, or equivalently for long enough propagation length, the diffusivity decreases exponentially and carriers enter the strong localization regime. Figure 6A and B shows the diffusivity of the defective 2DCPs with 0.5% and 2.0% monomer vacancies, respectively, as a function of propagation time and for an energy range encompassing the π and π^* bands. It is obvious from this picture that the diffusivity is strongly reduced in absolute value with increasing density of vacancy denoting the global degradation of transport properties which are described in more details in the following. At first, we report on the elastic mean free path and the semi-classical carrier mobility, i.e. l_e and μ_{sc}, that are semi-classical quantities deduced from the maximum of diffusivity curves. Then, the impact of quantum interferences is assessed and localization phenomena are discussed later.

The calculated elastic mean free path (l_e) is plotted in Figure 4B. The maximum of l_e is reached just after the van Hove singularity ($E \sim \pm 0.3$ eV), and drops rapidly to values close to zero at the Dirac point ($E = 0$ eV) and at the band extrema ($E \sim \pm 0.7$ eV). Even at defect concentrations as high as 2% the elastic mean free path is around 50 nm, and it surpasses 200 nm for 0.5% vacancies. The results associated to the mean free path suggest a tendency to follow the Fermi golden rule and could therefore be evaluated for any concentration as $\mathrm{l}_e^{[n_v]}$=$\mathrm{l}_e^{[n_v^0]}\frac{n_v^0}{n_v}$. A good fit for dependence in energy of $l_e^{[1\%]}$ is given by $\mathrm{l}_e^{[1\%]}(E)$= $A_0\,|sin(A_1\,E)| + A_2\,E^2 + A_3\,E^4 + A_4\,E^6$, with A_0=404.27, A_1=-2.17933, A_2=-1706.07, A_3=4000.87, A_4 =-3972.53. This fit was used to determine $\mathrm{l}_e^{[0.5\%]}$ and $\mathrm{l}_e^{[2.0\%]}$ in Figure 4B (black dotted lines) which confirms the straightforward relation between defect densities and transport properties.

The charge carriers mobility (μ) can be evaluated as $\mu(E_F,T)$=$(\sigma(E_F,T))/(e\,n(E_F,T))$, where e is the elementary charge, σ is the conductivity, and $n(E_F,T)$ is the charge carrier density which is defined as

$$n(E_F,T) = \left[\int_{-\infty}^{E_D} \rho(E)\left(1 - f^{\mathrm{FD}}(E,E_F,T)\right)dE\right] - \left[\int_{E_D}^{+\infty} \rho(E) f^{\mathrm{FD}}(E,E_F,T) dE\right] \quad (1)$$

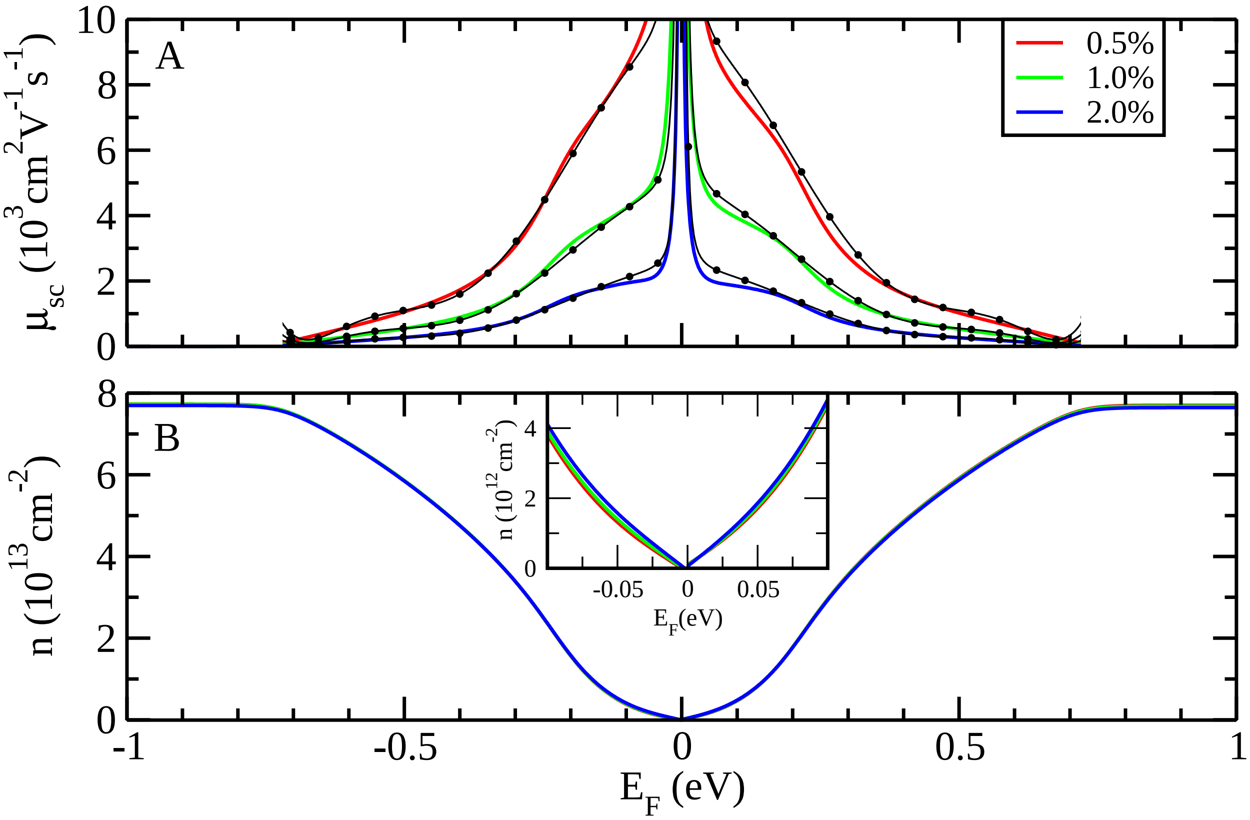

Figure 5: (A) Charge carrier mobilities ($\mu_{\rm sc}$) and (B) charge carrier densities (n) in the defective 2DCP monolayers as a function of the Fermi energy (E_F).

where $f^{\mathrm{FD}}(E, E_F, T)$ is the Fermi-Dirac distribution function for a given Fermi energy E_F and temperature T. $\rho(E)$ is the DOS per unit of area, and E_D=0 eV is the Dirac point energy. The semi-classical mobility (μ_{sc}) is evaluated using the semi-classical conductivity (σ_{sc}) (see method section).

Figure 5 displays the semi-classical mobility and charge density at room temperature (T=300K). By definition μ is inversely proportional to n, and the value of the mobility diverges when n tends to zero. Away from this divergence, the semi-classical mobilities are found in the range [2-8] 10^3 $\mathrm{cm^2V^{-1}s^{-1}}$ for concentration n_v ranging from 2.0 to 0.5% respectively. Such values of mobilities are high enough to envision electronic devices based on 2DCPs. However, they do not account for other sources of elastic scattering such as charged impurities trapped in the oxide substrate and neither inelastic scattering coming for instance from electron-phonon coupling at finite temperature, which are beyond the scope of the present paper. As for mean free path, $\mu_{\mathrm{sc}}^{[1\%]}$ can be fitted and used to determine the mobility at any concentration following Fermi golden rule (black dotted line in Fig.5A). The fit for the energy dependence of $\mu_{\mathrm{sc}}^{[1\%]}$ is given by $\mu_{sc}^{[1\%]}(E) = A_0/E^2 + A_1 + A_2\,E^2 + A_3\,E^4 + A_4\,E^6 + A_5\,E^8$, with A_0=1.09806, A_1=4595.83, A_2=-52860.3, A_3=262905, A_4=-580563, A_5=462335. The properties discussed above, i.e. l_e and μ_{sc}, are semi-classical quantities that do not account for quantum interferences and carriers localization. From Figure 6A and B, it seems that time dependent diffusivity saturates at a maximal value indicating a semi-classical regime and the absence of quantum correction. However, when re-scaling the diffusivity to its maximal value and looking closer to the zero energy region (Fig.6C and D), it turns out that localization effects emerge in the vicinity of the Dirac point. Although those effects are rather small for n_v=0.5%, the impact of interferences is much clearer for n_v=2.0%. For n_v=2.0%, the energy window corresponding to localization is in the range of 50 meV and displays a sharp transition between localized and semi-classical regimes indicating a rapidly varying localization length.

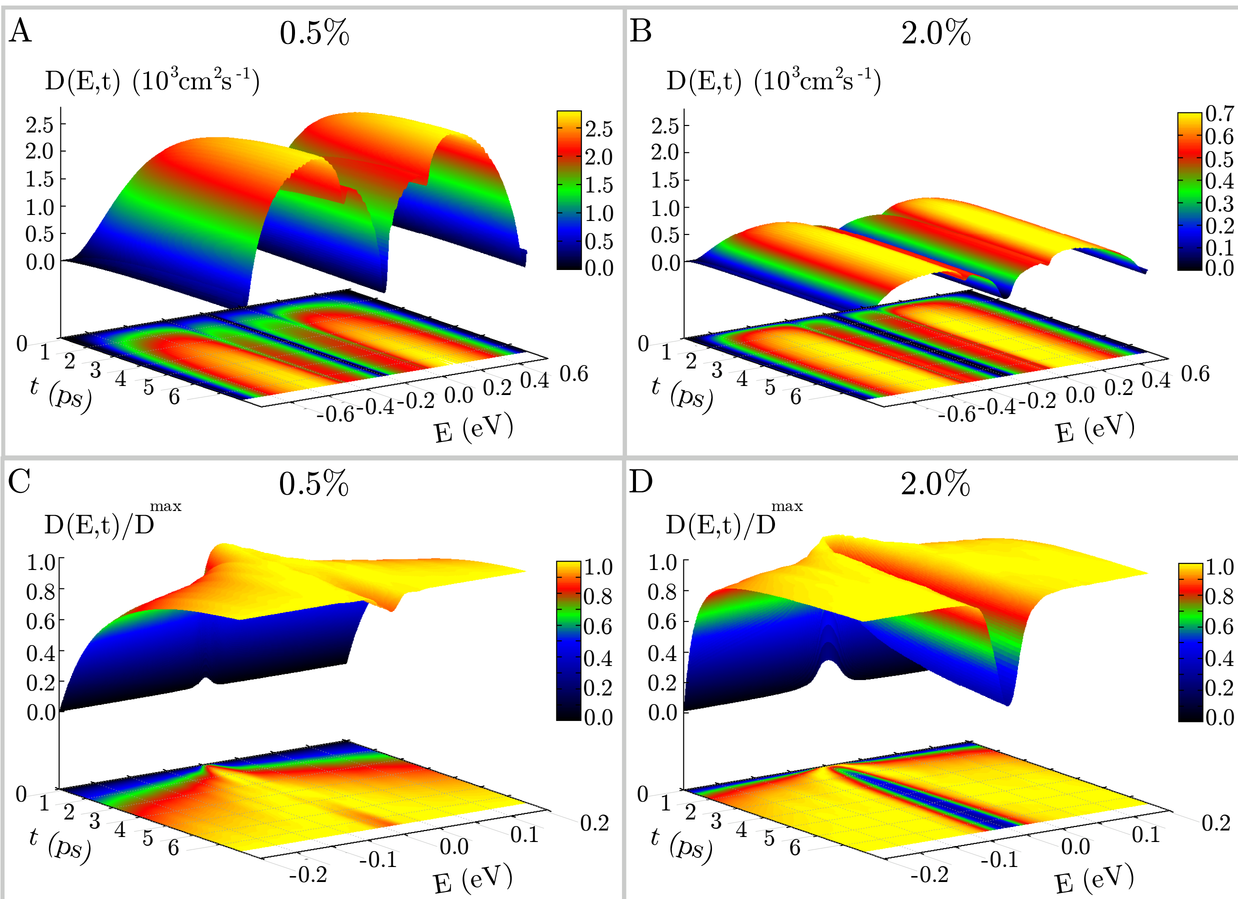

Figure 6: 3D plots of the diffusivity as a function of time and energy for 2D-C-$(PP_1)_3$ with vacancy defect concentration of 0.5% (A) and 2.0% (B) respectively. (C) and (D) are the normalized diffusivity of (A) and (B) at smaller energy range.

Transport regimes

In order to obtain a deeper understanding of this sharp transition between localized and semi-classical transport regimes, we calculated the inverse participation ratio (IPR) which measures the degree of localization of a wave function. For an ideally localized wave function, i.e. localized on a single orbital j, IPR is equal to 1. Inversely, the IPR of an ideally delocalized wave function equals to $1/N_{\mathrm{orb}}$. Figure 7A shows the IPR for a pristine and a defective 2DCP 16×16 super cell. Interestingly, for a pristine 2DCP, the wave function is not fully delocalized (Fig. 7A). This is further highlighted in supplementary Figure 1B where the wave function of a pristine 2DCP is calculated for the K-point of the Brillouin zone at the Fermi energy. For a concentration of defects of 1.56%, the degree of localization increases as expected and is almost twice the IPR value of the pristine case at energies away from the Fermi level. For energies around the Fermi level, the IPR varies to show an increase in localization with its maximum at E_F=0 eV. The effects of localization on charge carrier mobility is highlighted in Figure 7B. One observes that the semi-classical mobility μ_{sc}, see also Figure 5, strongly varies around the Dirac point as a function of the temperature (black dashed dotted and dashed lines). The quantum mobility (at T=0K and accounting for possible quantum interferences) increases as a function of the propagation length and saturates to μ_{sc}(T=0K) for energies outside the localization window. Around the Dirac point, localization effects are at stake and the quantum mobility vanishes for large enough propagation lengths. These two opposite behaviors create sharp variations of mobility, called mobility edges, around energies indicated by the arrows in Fig. 7B. Figure 7A-B corroborates the strong localization around the Fermi energy and the two different behaviors leading to the mobility edge in 2DCP. Such a mobility edge is signature of the separation between transport regimes based on extended and localized states and is a priori only expected in 3D materials.[16] However, it has been shown that the nature of disorder plays an important role in this commonly accepted prediction and that mobility edge can actually be induced in low-dimensional materials.[25,26] This explains why such mobility edge signature is highly

300 sought in 1D and 2D systems. Similar semimetal-insulator transitions were also reported in
301 graphene.[27,28]

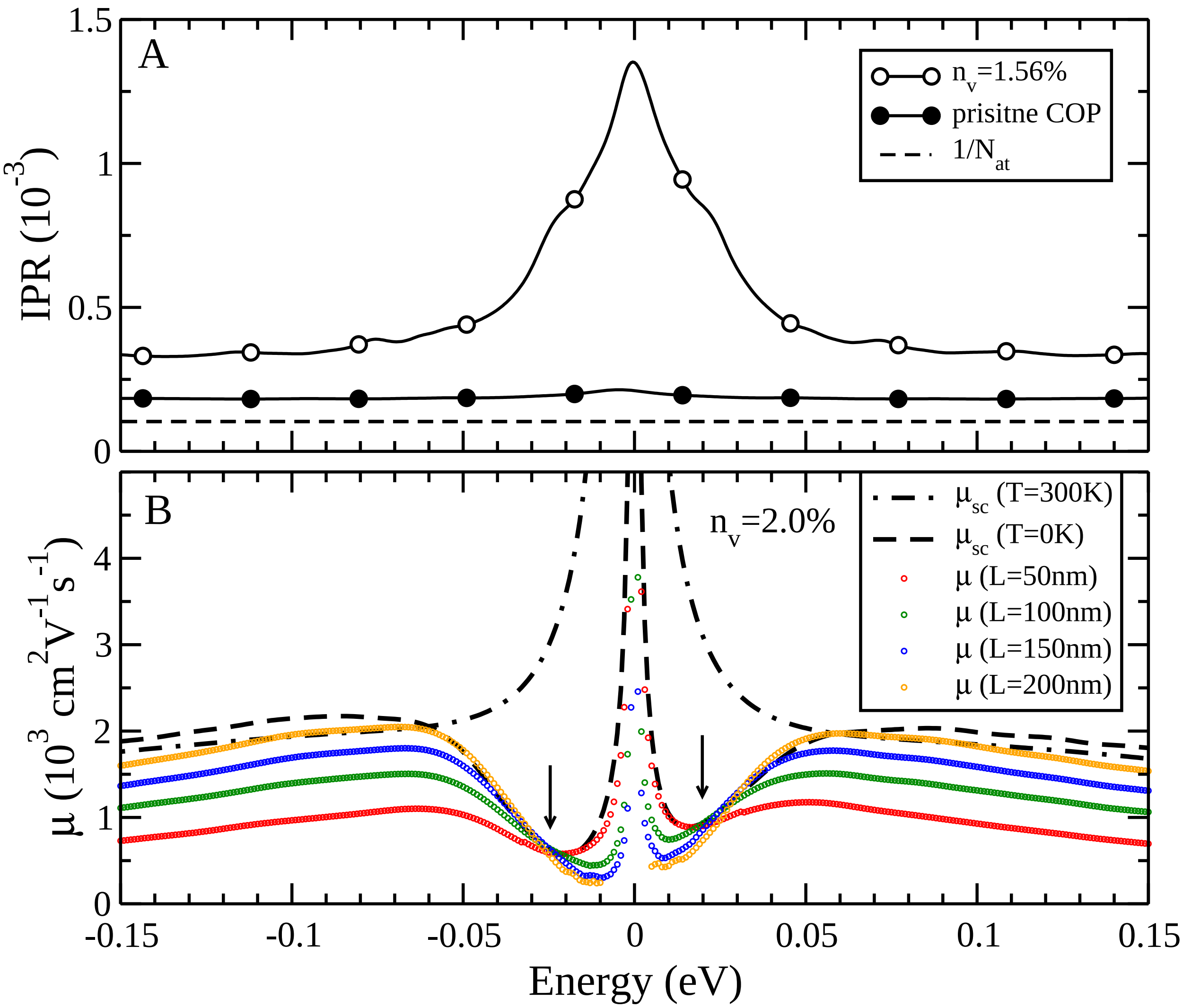

Figure 7: (A) Inverse participation ratio (IPR) for an ideal delocalized wave function (dashed line), for a pristine (black circle), and for a 1.56% defects (white circle) 2DCP; (B) the mobilities in the semi-classical (μ_{sc}) and in the quantum (μ) regime for a 2DCP containing n_v=2.0% of randomly distributed vacancies.

302 ## Conclusions

303 The electronic structures of 2DCPs share various similarities with graphene, notably the
304 linear energy dispersion giving rise to massless Dirac fermions characteristics around the

Fermi energy. However, the major differences are the energy bandwidth and the complete isolation of the fully symmetric $\pi - \pi^*$ bands. This makes the 2D-C-$(PP_1)_3$ an interesting material to probe the transport properties of π-π^* manifold. It is predicted that the bottom (top) of the π valence (π^* conduction) band could be accessible in a transport experiment using an appropriate high-κ dielectric as gate oxide. These structures are robust to chemical doping and retain the linear dispersive bands upon large variations of charge density. The transport properties of realistic large 2DCP sheets containing randomly distributed monomer vacancy defects have been investigated. The carriers exhibit good transport properties with long mean free paths and high mobilities (in the range 10^3 cm^2 V^{-1} s^{-1}) allowing to envision 2DCP-based electronic devices. Sharp variation of the low temperature mobility around the Dirac point are reported for systems containing large concentration of defects indicating the possibility to observe a mobility edge in 2DCPs. As the 2DCPs topology gives them a flexibility which might not be accessible to graphene, the peculiar electronic and transport properties reported in this study are expected to stimulate further research on these new materials in view of their implementation in future polymer-based electronic devices.

Methods

Ab initio approach

Ab initio calculations have been performed using the Siesta package.[17,18] The exchange-correlation energy and electron-ion interaction are described using GGA-PBE[29] functional and norm-conserving pseudopotentials[30] in the fully non local form, respectively. A double-ζ polarized basis set of numerical atomic orbitals is used and the energy cutoff for real-space mesh is set to 300 Ry. A Fermi-Dirac distribution function with an electronic temperature of 10 meV is used to populate the energy levels. The geometries are fully relaxed until the forces on each atom and on the unit cell are less than 0.01 and 0.03 eV/Å, respectively. Periodic boundaries were applied with inter-layer vacuum distance >10 Å for single layers.

A fine k-point grid of at least 20×20×1 for monolayers was chosen using Monkhorst-Pack scheme.[31] Atomic positions and lattice parameters were geometrically optimized prior to band structure calculations. All these parameters ensured the convergence of the ground state properties (geometric and electronic structures) to less than one meV/atom.

Tight-binding model

Tight-binding calculations have been performed using the TB_Sim package. The hopping terms are distant-dependent and reads as $\gamma(d) = \pm\gamma_0 e^{-3.37\left(\frac{d}{d_{\mathrm{CC}}}-1\right)}$ where d_{CC}=1.42 Å is the stable sp^2 carbon-carbon distance, and d is the interatomic distance of a given carbon atoms pair with a cutoff of ∼3.2Å accounting therefore up to the third nearest neighbors. The sign (±) in this formula is negative only for second nearest neighbors This parametrization has been performed by fitting the *ab initio* band structure described in Figure 1C. The same TB parametrization stands for the 2×2 super-cell containing a monomer vacancy defect, meaning that no special treatment is performed for the carbon atoms which are left with a missing neighboring carbon atoms which we thus considered to be saturated by hydrogen in the experiment.

Table 1: *Tight-binding* parameters of the pristine 2DCP. Two carbon species are accounted for in this model, depending on whether they are hydrogenated edge atoms (C_2), or not (C_1). The on-site terms (ϵ) of each carbon species is given first, followed by the hopping terms (γ_0) as defined in the text. All the energy terms are given in eV.

	on-site terms (ϵ)
C_1	0.00
C_2	-0.60
	hopping terms (γ_0)
C_1-C_1	-3.55
C_1-C_2	-2.85
C_2-C_2	-2.55

Transport methodology

The transport properties are computed from the dynamics of propagating electronic wavepackets with a real-space Kubo-Greenwood method described in details in Refs.[14,32,33] The dynamics is monitored through the time-dependent diffusivity coefficient $D(E,t) = \Delta R^2(E,t)/t$, with E the energy of the carriers, $\Delta R^2 = \Delta X^2 + \Delta Y^2$, and $\Delta X^2(E,t)=\mathrm{Tr}[\delta(E-\hat{H})|\hat{X}(t)-\hat{X}(0)|^2]/\mathrm{Tr}[\delta(E-\hat{H})]$ the quadratic spreading along the x direction. Tr is the trace over p_z orbitals and $\mathrm{Tr}[\delta(E-\hat{H})]/S = \rho(E)$ is the total DOS (per unit of surface S). The results are averaged over multiple initial random phase wavepackets. The transport properties are inferred from the time evolution of $D(E,t)$. At very short times, the wavepacket dynamics is quasi-ballistic, so that $D(E,t) \propto \nu^2(E)t$, where $\nu(E)$ is the carrier velocity. The dynamics further becomes diffusive as the carriers get scattered by the disorder, and $D(E,t)$ reaches a maximum value $D^{\max}(E) = 2\nu(E)l_e(E)$, where $l_e(E)$ is the mean free path. The semi-classical conductivity then reads $\sigma_{\mathrm{sc}}(E)=(1/4)e^2\rho(E)D^{\max}(E)$. All the simulations are conducted at 0 K meaning that the electronic transport is fully coherent. However, it is possible to account for a physical temperature in the evaluation of σ through the use of Fermi-Dirac distribution. $\sigma_{\mathrm{sc}}(E_F,T)=-\frac{1}{4}e^2\int_{-\infty}^{+\infty}\rho(E)\;D^{\max}(E)\frac{\partial f^{\mathrm{FD}}(E,E_F,T)}{\partial E}$. The semi-classical mobility is then defined as $\mu_{\mathrm{sc}}(E_F,T)=(\sigma_{\mathrm{sc}}(E_F,T))/(e\,n(E_F,T))$ where $n(E_F,T)$ is the charge carrier density. At longer propagation times weak localization corrections due to multiple scattering events per carrier can cause $D(E,t)$ to decrease and possibly vanish when reaching the strong localization regime. To describe evolution of the conductivity and mobility in the transient regime, either between ballistic and diffusive regimes, or between diffusive or localized regime, one can defines σ and μ at any propagation time or equivalently at any propagation length using $D(E,t)$ instead of $D^{\max}(E)$. The conductivity and the mobility become then extensive quantities which now depend on L computed from the spreading of wave packets as $L=2\sqrt{\Delta R^2(t,E)}$.

Inverse participation ratio

The inverse participation ratio (IPR) is a measure of the localization of the eigenstates. For a particular eigenstate ψ^{α}, it is defined as

$$\mathrm{IPR}_{\alpha} = \frac{\sum_{\mathrm{i=1}}^{\mathrm{N_{orb}}} |\psi_{\mathrm{i}}^{\alpha}|^4}{|\sum_{\mathrm{i=1}}^{\mathrm{N_{orb}}} |\psi_{\mathrm{i}}^{\alpha}|^2|^2} \tag{2}$$

where N_{orb} is the number of orbitals. In the present TB model, it is equal to the number of atoms N_{at}. For normalized eigenstates ($\sum_{i=1}^{N_{\mathrm{orb}}} |\psi_i^{\alpha}|^2 = 1$) this reduces to $\mathrm{IPR}_{\alpha} = \sum_{\mathrm{i=1}}^{\mathrm{N_{orb}}} |\psi_{\mathrm{i}}^{\alpha}|^4$. This quantity can be integrated over the Brillouin zone to evaluate the energy-dependent IPR. For a wave function localized on a single orbital j, $\psi_i^{\alpha} = 0$ for $i \neq j$, and hence IPR=1. For a perfectly delocalized wave function on all orbital, ψ_i^{α} has an equal weight on each orbital $\frac{1}{\sqrt{N_{\mathrm{orb}}}}$, and hence IPR=$\frac{1}{N_{\mathrm{orb}}}$.

Acknowledgement

A.L., S.D., A.R.B.M. and J.-C.C. acknowledge financial support from the Fonds de la Recherche Scientifique de Belgique (F.R.S.-FNRS), from the Communauté Wallonie-Bruxelles through the Action de Recherche Concertée (ARC) on Graphene Nano-electromechanics (no. 11/16-037) and from the European ICT FET Flagship entitled "Graphene-based revolutions in ICT and beyond".(no. 604391). J.-J.A. acknowledges support from the Marcel De Merre Prize. Computational resources have been provided by the supercomputing facilities of the Université catholique de Louvain (CISM/UCL) and the Consortium des Equipements de Calcul Intensif en Fédération Wallonie Bruxelles (CECI) funded by the F.R.S.-FNRS.

References

(1) Novoselov, K. S.; Geim, A. K.; Morozov, S. V.; Jiang, D.; Zhang, Y.; Dubonos, S. V.; Grigorieva, I. V.; Firsov, A. A. *Science* **2004**, *306*, 666.

(2) Novoselov, K. S.; Geim, A. K.; Morozov, S. V.; Jiang, D.; Katsnelson, M. I.; Grigorieva, I. V.; Dubonos, S. V.; Firsov, A. A. *Nature* **2005**, *438*, 197.

(3) Kishigi, K.; Ueno, K.; Miyamoto, E.; Hasegawa, Y. *Journal of Physics: Conference Series* **2011**, *334*, 012047.

(4) Cai, J.; Ruffieux, P.; Jaafar, R.; Bieri, M.; Braun, T.; Blankenburg, S.; Muoth, M.; Seitsonen, A.; Saleh, M.; Feng, X.; Müllen, K.; Fasel, R. *Nature* **2010**, *466*, 470–473.

(5) Adjizian, J.-J.; Briddon, P.; Humbert, B.; Duvail, J.-L.; Wagner, P.; Adda, C.; Ewels, C. *Nature Communications* **2014**, *5*, 5842.

(6) Côté, A. P.; Benin, A. I.; Ockwig, N. W.; O'Keeffe, M.; Matzger, A. J.; Yaghi, O. M. *Science* **2005**, *310*, 1166–1170.

(7) Feldblyum, J.; McCreery, C.; Andrews, S.; Kurosawa, T.; Santos, E.; Duong, V.; Fang, L.; Ayzner, A.; Bao, Z. *Chemical Communications* **2015**, *51*, 13894.

(8) Xiang, Z.; Cao, D. *Macromol Rapid Commun.* **2012**, *33*, 1184.

(9) Xiang, Z.; Cao, D.; Huang, L.; Shui, J.; Wang, M.; Dai, L. *Advanced Materials* **2014**, *26*, 3315.

(10) Mendoza-Cortes, J.; Han, S.; Furukawa, H.; Yaghi, O.; Goddard, W. A. *The journal of physical chemistry A* **2010**, *114*, 10824–10833.

(11) Wan, S.; Guo, J.; Kim, J.; Ihee, H.; Jiang, D. *Angewandte Chemie, International Edition* **2008**, *47*, 8826–8830.

(12) Pereira, V.; dos Santos, J. L.; Castro-Neto, A. *Physical Review B* **2008**, *77*, 115109.

(13) Yazyev, O. V.; Louie, S. *Nature Materials* **2010**, *9*, 806.

(14) Lherbier, A.; Dubois, S.; Declerck, X.; Niquet, Y.-M.; Roche, S.; Charlier, J.-C. *Physical Review B* **2012**, *86*, 075402.

(15) Cresti, A.; Ortmann, F.; Louvet, T.; Tuan, D. V.; Roche, S. *Physical Review Letters* **2013**, *110*, 196601.

(16) Lee, P. A.; Ramakrishnan, T. V. *Rev. Mod. Phys.* **1985**, *57*, 287–337.

(17) Soler, J. M.; Artacho, E.; Gale, J. D.; Garca, A.; Junquera, J.; Ordejon, P.; Sanchez-Portal, D. *Journal of Physics: Condensed Matter* **2002**, *14*, 2745.

(18) Artacho, E.; Anglada, E.; Dieguez, O.; Gale, J. D.; Garca, A.; Junquera, J.; Martin, R. M.; Ordejon, P.; Pruneda, J. M.; Sanchez-Portal, D.; Soler, J. M. *Journal of Physics: Condensed Matter* **2008**, *20*, 064208.

(19) Botello-Méndez, A.; Lherbier, A.; Charlier, J.-C. *Solid State Communications* **2013**, *175-176*, 90–100.

(20) Lherbier, A.; Botello-Méndez, A.; Charlier, J.-C. *Nano Letters* **2013**, *13*, 1446.

(21) Brouwer, P. W.; Racine, E.; Furusaki, A.; Hatsugai, Y.; Morita, Y.; Mudry, C. *Physical Review B* **2002**, *66*, 014204.

(22) Castro-Neto, A. H.; Guinea, F.; Peres, N. M. R.; Novoselov, K. S.; Geim, A. K. *Reviews of modern physics* **2009**, *81*, 109–162.

(23) Meric, I.; Han, M.; Young, A.; Ozyilmaz, B.; Kim, P.; Shepard, K. *Nature Nanotechnology* **2008**, *3*, 654.

(24) Haydock, R. *Computer Physics Communications* **1980**, *20*, 11 – 16.

(25) Das Sarma, S.; He, S.; Xie, X. C. *Phys. Rev. Lett.* **1988**, *61*, 2144–2147.

(26) Naumis, G. G. *Phys. Rev. B* **2007**, *76*, 153403.

(27) Leconte, N.; Moser, J.; Ordejón, P.; Tao, H.; Lherbier, A.; Bachtold, A.; Alsina, F.; Torres, C. S.; Charlier, J.-C.; Roche, S. *ACS Nano* **2010**, *4*, 4033–4038.

(28) Skrypnyk, Y. V.; Loktev, V. M. *Phys. Rev. B* **2011**, *83*, 085421.

(29) Perdew, J. P.; Burke, K.; Ernzerhof, M. *Physical Review Letters* **1996**, *77*, 3865.

(30) Troullier, N.; Martins, J. L. *Physical Review B* **1991**, *43*, 1993.

(31) Monkhorst, H.; Pack, J. *Physical Review B* **1976**, *13*, 5188.

(32) Roche, S.; Mayou, D. *Physical review letters* **1997**, *79*, 2518.

(33) Leconte, N.; Lherbier, A.; Varchon, F.; Ordejón, P.; Roche, S.; Charlier, J.-C. *Physical review B* **2011**, *84*, 235420.